# ANALYTICAL METHODS FOR MODELING INFLOW DYNAMICS OF A COAXIAL ROTOR SYSTEM

**J. V. R. Prasad** jvr.prasad@ae.gatech.edu
**Yong-Boon Kong** kyongboo@gatech.edu
School of Aerospace Engineering
Georgia Institute of Technology
Atlanta, Georgia, USA

**David Peters** dap@wustl.edu
Mechanical Eng. & Materials Sci.
Washington University
Saint Louis, Missouri, USA

## Abstract

For real-time rotor inflow calculations, finite state inflow models are often used due to the fact that they are more computationally efficient compared to CFD models. Single rotor pressure and velocity potential inflow models have been shown to correctly predict induced velocities across a rotor disk. Both models are formulated from an incompressible potential flow solution and assume a rigid cylindrical wake structure. An extension of single rotor inflow models to a coaxial rotor system by superposition method is explored in this paper. In the velocity potential superposition method, rotor-to-rotor interactions are considered through individual rotor loads. For the pressure potential superposition approach, the coupling between upper and lower rotors are done through the apparent mass matrix (M-matrix) and the inflow influence coefficient matrix (L-matrix). The resulting two inflow models for a coaxial rotor system are compared using their response predictions both in time and frequency domains. Differences in transient responses between the two models are found when subjected to step perturbations on individual rotor loadings of a coaxial rotor system. In addition, significant phase differences between the models are observed in their frequency responses. The differences in transient responses between the two models can be attributed to the fact that it takes finite time for upper rotor inflow perturbations to propagate to the lower rotor, which is captured in the velocity potential superposition method as opposed to the pressure potential superposition method.

## 1. NOMENCLATURE

| | |
|---|---|
| $[D]$ | Damping matrix |
| $[L], [\tilde{L}]$ | Influence coefficient matrix |
| $[M], [\tilde{M}]$ | Apparent mass matrix |
| M, N | Total number of harmonics and radial terms |
| $[V_m]$ | Mass flow parameter |
| $V_\infty$ | Free-stream velocity, ft/s |
| $V_T$ | Total average flow at the rotor, $\sqrt{(V_\infty \sin\chi)^2 + (V_\infty \cos\chi + \bar{v}_z)^2}$ ft/s |
| $\bar{P}_n^m, \bar{Q}_n^m$ | Normalized Legendre function of the first and second kind, respectively |
| R | Radius of rotor, ft |
| $a, a^*$ | Velocity and adjoint velocity states, respectively |
| m, r | Harmonic number |
| n, j | Polynomial number |
| $\bar{r}$ | Radial position normalized with respect to rotor radius |
| $t$ | Time, seconds |
| $\bar{t}$ | Reduced time, $V_\infty t/R$ |
| $\vec{v}$ | Velocity vector |
| $\vec{v}^*$ | Adjoint velocity vector |
| $\bar{v}_z$ | Induced downwash normalized with respect to blade tip speed |
| $\bar{x}, \bar{y}, \bar{z}$ | Cartesian coordinates normalised by R |
| $z_{sep}$ | Separation distance between the upper and lower rotors, ft |
| $\alpha_j^r, \beta_j^r$ | Inflow states corresponding to cosine and sine components, respectively |
| $\chi$ | Momentum wake skew angle, $\tan^{-1}\left(\frac{\mu}{\lambda_f + \lambda_m}\right)$ rads |
| $\lambda_f$ | Inflow due to free-stream normalised with respect to blade tip speed |
| $\lambda_m$ | Total induced inflow at rotor normalised with respect to blade tip speed |
| $\vec{\nabla}$ | Gradient operator |

| | |
|---|---|
| $\nu, \eta, \psi$ | Ellipsoidal coordinates |
| $\Psi_n^m$ | Inflow shaping function |
| $\hat{\Psi}_n^m$ | Derived velocity potentials |
| $\phi$ | Pressure potential |
| $\tau_n^{mc}, \tau_n^{ms}$ | Pressure coefficients of cosine and sine components |
| $\xi$ | Streamline coordinates |

## 2. INTRODUCTION

For single rotor configurations, the Peters-He finite state inflow model[1] provides an efficient and accurate means to calculate inflow distributions across the rotor. It models the rotor disk as a pressure potential source and computes the resulting induced inflow across the rotor. Peters-He finite state inflow model is widely used in standard software such as FLIGHTLAB® [2] and RCAS[3] for rotorcraft simulations. Recently, using a velocity potential representation of the flow field[4,5,6], the finite state inflow model has been reformulated to predict all three components of flow velocities both on and off the rotor disk. Results from this new velocity potential inflow model has been shown to agree well with exact solutions.

In the modeling of inflow for a coaxial rotor system, superposition of single rotor inflow models can be utilised. For velocity potential superposition method, inflow dynamics of each rotor is assumed to be independent from each other, and rotor-to-rotor flow field coupling is done through individual rotor loads. This makes the extension of velocity potential superposition to a multi-rotor configuration to be somewhat straightforward. A key aspect of the velocity potential model is that one needs to solve both the velocity as well as the adjoint velocity states (co-states) in order to compute flow velocities inside the rotor wake, thus doubling the number of equations to be solved. Moreover, because of the negative sign in the apparent mass matrix of the adjoint model, one needs to integrate the adjoint equations backward in time, making it challenging for real time simulation.

In the method based on superposition of individual rotor pressure fields, superposition of the pressure potentials associated with the individual rotors of a coaxial rotor system is considered[7,8,9]. The inflow dynamics at each rotor is affected by its own and other rotor's pressure potential. In this case, rotor-to-rotor coupling is affected through the apparent mass matrix (M-matrix) and inflow influence coefficient matrix (L-matrix). Due to the tight coupling between the inflow dynamics of upper and lower rotors through these matrices, extension of pressure potential inflow model to a multi-rotor system is not a trivial task. On the other hand, pressure potential inflow model does not involve adjoint velocity states, and hence, does not require backward time marching to compute the solutions. As such, it can easily be integrated into a rotorcraft flight simulation model.

The main objective of this paper is to compare the pressure potential superposition and velocity potential superposition methods for modeling of inflow dynamics of a coaxial rotor configuration. First, analytical approaches of the two methods, viz., pressure potential superposition and the velocity potential superposition methods, are presented. Next, transient responses of the resulting models are compared both in time and frequency domains.

## 3. MODELLING

Both velocity and pressure potential flow models assume that the flow field is inviscid, irrotational and incompressible. In addition, the wake geometry in both models are rigid and cylindrical in shape. In forward flight, a skewed cylindrical wake with an average wake skew angle based on momentum theory is used. This section describes the modeling approaches based on pressure potential and velocity potential superposition for coaxial rotor configurations.

### 3.1. Pressure potential superposition inflow model

Pressure potential inflow model is formulated from continuity and momentum equations of an incompressible potential flow representation given as,

$$\vec{\nabla} \cdot \vec{v} = 0 \tag{1}$$

$$\frac{\partial \vec{v}}{\partial t} - V_\infty \frac{\partial \vec{v}}{\partial \xi} = -\vec{\nabla}\phi \tag{2}$$

The on-disk inflow is modelled by using shaping functions, $\Psi_n^m$ with associated cosine and sine harmonics and weighting coefficients.

$$\bar{v}_z = \sum_r^M \sum_{j=r+1,r+3\ldots}^N \Psi_j^r(\nu)[\alpha_j^r \cos(r\psi) + \beta_j^r \sin(r\psi)] \tag{3}$$

$$\Psi_j^r(\nu) = \frac{\bar{P}_j^r(\nu)}{\nu} \tag{4}$$

In addition, the pressure term $\phi$, in equation (2) is expanded in terms of Legendre polynomials and harmonic functions.

$$\phi = \sum_{m}^{M} \sum_{n=m+1,m+3\ldots}^{N} \bar{P}_n^m(\nu)\bar{Q}_n^m(\eta) \left[\tau_n^{mc}\cos(m\psi) + \tau_n^{ms}\sin(m\psi)\right] \tag{5}$$

By considering the pressure field to be the sum of individual pressure fields of the upper and lower rotors, and using the shaping function expansion of induced velocities at the upper and lower rotors, the relationship between inflow states and pressure coefficients is obtained after substituting equations (3) through (5) into equation (2). The resulting set of equations can be written as[9],

$$\begin{bmatrix} M_{11} & M_{12} \\ M_{21} & M_{22} \end{bmatrix} \begin{Bmatrix} \dot{\alpha_1} \\ \dot{\alpha_2} \end{Bmatrix} + [V_m] \begin{bmatrix} L_{11} & L_{12} \\ L_{21} & L_{22} \end{bmatrix}^{-1} \begin{Bmatrix} \alpha_1 \\ \alpha_2 \end{Bmatrix} = \begin{Bmatrix} \tau_1/2 \\ \tau_2/2 \end{Bmatrix} \tag{6}$$

In equation (6), $\alpha_1$ and $\alpha_2$ correspond to column vectors of inflow states of upper rotor (denoted as 1) and lower rotor (denoted as 2), respectively. The pressure coefficients $\tau_1$ and $\tau_2$ are vector coefficients of pressure fields of upper and lower rotors, respectively. Each M-block in the equations is a matrix of apparent mass effect terms relating inflow state dynamic responses to perturbations in pressure coefficients. The blocks $M_{11}$ and $M_{22}$ are the same as the M-matrix in Peters-He inflow model while each element in blocks $M_{12}$ and $M_{21}$ are found through numerical integration of equations (7) though (12).

By definition, the M-matrix is inverse of the E operator such that $[M] = [E]^{-1}$. Each element in $[E_{12}]$ is,

$$E_{jn,\cos}^{0m} = \frac{1}{2\pi}\int_0^{2\pi}\int_0^1 \Psi_j^0(\nu_1) * \frac{\partial(\bar{P}_n^m(\nu_2)\bar{Q}_n^m(\eta_2)\cos(m\psi_2))}{\partial z_1} d\nu_1 d\psi_1 \tag{7}$$

$$E_{jn,\cos}^{rm} = \frac{1}{\pi}\int_0^{2\pi}\int_0^1 \Psi_j^r(\nu_1)\cos(r\psi_1) * \frac{\partial(\bar{P}_n^m(\nu_2)\bar{Q}_n^m(\eta_2)\cos(m\psi_2))}{\partial z_1} d\nu_1 d\psi_1 \tag{8}$$

$$E_{jn,\sin}^{rm} = \frac{1}{\pi}\int_0^{2\pi}\int_0^1 \Psi_j^r(\nu_1)\sin(r\psi_1) * \frac{\partial(\bar{P}_n^m(\nu_2)\bar{Q}_n^m(\eta_2)\sin(m\psi_2))}{\partial z_1} d\nu_1 d\psi_1 \tag{9}$$

By changing variables related to rotor 1 with rotor 2 and vice-versa, elements in $[E_{21}]$ is given by,

$$E_{jn,\cos}^{0m} = \frac{1}{2\pi}\int_0^{2\pi}\int_0^1 \Psi_j^0(\nu_2) * \frac{\partial(\bar{P}_n^m(\nu_1)\bar{Q}_n^m(\eta_1)\cos(m\psi_1))}{\partial z_2} d\nu_2 d\psi_2 \tag{10}$$

$$E_{jn,\cos}^{rm} = \frac{1}{\pi}\int_0^{2\pi}\int_0^1 \Psi_j^r(\nu_2)\cos(r\psi_2) * \frac{\partial(\bar{P}_n^m(\nu_1)\bar{Q}_n^m(\eta_1)\cos(m\psi_1))}{\partial z_2} d\nu_2 d\psi_2 \tag{11}$$

$$E_{jn,\sin}^{rm} = \frac{1}{\pi}\int_0^{2\pi}\int_0^1 \Psi_j^r(\nu_2)\sin(r\psi_2) * \frac{\partial(\bar{P}_n^m(\nu_1)\bar{Q}_n^m(\eta_1)\sin(m\psi_1))}{\partial z_2} d\nu_2 d\psi_2 \tag{12}$$

Under steady-state condition, the blocks $L_{11}$ and $L_{22}$ relate self-induced inflows to the aerodynamic loading on each rotor which is the same as a single rotor Peters-He L-matrix. The blocks $L_{12}$ and $L_{21}$ relate inflow coupling between the two rotors where the elements in each block are given in equations (13) through (18).

For the elements in $[L_{12}]$,

$$L_{jn,\cos}^{0m} = \frac{1}{2\pi}\int_0^{2\pi}\int_0^1 \Psi_j^0(\nu_1) * \int_0^\infty \frac{\partial(\bar{P}_n^m(\nu_2)\bar{Q}_n^m(\eta_2)\cos(m\psi_2))}{\partial z_1} d\xi_2 d\nu_1 d\psi_1 \tag{13}$$

$$L_{jn,\cos}^{rm} = \frac{1}{\pi}\int_0^{2\pi}\int_0^1 \Psi_j^r(\nu_1)\cos(r\psi_1) * \int_0^\infty \frac{\partial(\bar{P}_n^m(\nu_2)\bar{Q}_n^m(\eta_2)\cos(m\psi_2))}{\partial z_1} d\xi_2 d\nu_1 d\psi_1 \tag{14}$$

$$L_{jn,\sin}^{rm} = \frac{1}{\pi}\int_0^{2\pi}\int_0^1 \Psi_j^r(\nu_1)\sin(r\psi_1) * \int_0^\infty \frac{\partial(\bar{P}_n^m(\nu_2)\bar{Q}_n^m(\eta_2)\sin(m\psi_2))}{\partial z_1} d\xi_2 d\nu_1 d\psi_1 \tag{15}$$

Similarly, for the elements in $[L_{21}]$,

$$L_{jn,\cos}^{0m} = \frac{1}{2\pi}\int_0^{2\pi}\int_0^1 \Psi_j^0(\nu_2) * \int_0^\infty \frac{\partial(\bar{P}_n^m(\nu_1)\bar{Q}_n^m(\eta_1)\cos(m\psi_1))}{\partial z_2} d\xi_1 d\nu_2 d\psi_2 \tag{16}$$

$$L_{jn,\cos}^{rm} = \frac{1}{\pi}\int_0^{2\pi}\int_0^1 \Psi_j^r(\nu_2)\cos(r\psi_2) * \int_0^\infty \frac{\partial(\bar{P}_n^m(\nu_1)\bar{Q}_n^m(\eta_1)\cos(m\psi_1))}{\partial z_2} d\xi_1 d\nu_2 d\psi_2 \tag{17}$$

(18) $$L^{rm}_{jn,\sin} = \frac{1}{\pi}\int_0^{2\pi}\int_0^1 \Psi^r_j(\nu_2)\sin(r\psi_2)* \int_0^\infty \frac{\partial(\bar{P}^m_n(\nu_1)\bar{Q}^m_n(\eta_1)\sin(m\psi_1))}{\partial z_2} d\xi_1 d\nu_2 d\psi_2$$

The subscripts "1" and "2" in equations (7) through (18) refer to the upper and lower rotor coordinate systems, respectively. As closed form expressions for these off-diagonal L-matrix blocks have not yet been found, they are pre-computed and stored in a lookup table indexed by average wake skew angle, $\chi$. Lastly, the pressure potential superposition inflow model assumes a rigid skewed cylindrical wake geometry with contraction effects taken into account. This is done by using a wake contraction table indexed by wake skew angle to correct the streamline coordinates.

### 3.2. Velocity potential superposition inflow model

The formulation of the velocity potential inflow model for single rotor configuration is described in Ref. 10 with the velocity ($\vec{v}$) and adjoint velocity ($\vec{v}^*$) represented by,

(19) $$\vec{v} = \sum_{m=0}^{\infty}\sum_{n=m}^{\infty}(a^{mc}_n\vec{\nabla}\hat{\Psi}^{mc}_n + a^{ms}_n\vec{\nabla}\hat{\Psi}^{ms}_n)$$
$$\vec{v}^* = \sum_{m=0}^{\infty}\sum_{n=m}^{\infty}(a^{*mc}_n\vec{\nabla}\hat{\Psi}^{mc}_n + a^{*ms}_n\vec{\nabla}\hat{\Psi}^{ms}_n)$$

In equation (19), $a$ and $a^*$ are column vectors of flow field velocity states and adjoint velocity states (co-states), respectively. The terms $\hat{\Psi}^c$ and $\hat{\Psi}^s$ are cosine and sine parts of the derived velocity potentials, respectively.

Now, the dynamic inflow model for a coaxial rotor configuration based on velocity potential superposition can be formulated by assuming that the flow dynamics of individual rotors are independent and the rotor-to-rotor flow field coupling is done through aerodynamic load changes of individual rotors. The resulting model can be written as,

(20) $$[\tilde{M}]\{\dot{a}\} + [D][\tilde{L}]^{-1}[\tilde{M}]\{a\} = [D]\{\tau\}$$

where

$$\tilde{M} := \begin{bmatrix}\tilde{M}_1 & 0 & 0 & 0\\ 0 & -\tilde{M}_1 & 0 & 0\\ 0 & 0 & \tilde{M}_2 & 0\\ 0 & 0 & 0 & -\tilde{M}_2\end{bmatrix}$$
$$D := \begin{bmatrix}D_1 & 0 & 0 & 0\\ 0 & D_1 & 0 & 0\\ 0 & 0 & D_2 & 0\\ 0 & 0 & 0 & D_2\end{bmatrix}$$
$$\tilde{L} := \begin{bmatrix}\tilde{L}_1 & 0 & 0 & 0\\ 0 & \tilde{L}_1 & 0 & 0\\ 0 & 0 & \tilde{L}_2 & 0\\ 0 & 0 & 0 & \tilde{L}_2\end{bmatrix}$$
$$a := \begin{Bmatrix}a_1\\ a^*_1\\ a_2\\ a^*_2\end{Bmatrix} \quad \tau := \begin{Bmatrix}\tau_1\\ \tau^*_1\\ \tau_2\\ \tau^*_2\end{Bmatrix}$$

In equation (20), $a_1$ and $a_2$ are column vectors of flow field velocity states (consist of cosine and sine terms) corresponding to upper and lower rotors, respectively while the terms $a^*_1$ and $a^*_2$ are the adjoint velocity states for upper and lower rotors, respectively. In addition, each element in $\tau^*$ is defined as $(-1)^{n+1}\tau^m_n$. While closed-form solutions for the elements in matrix $\tilde{M}$, D and $\tilde{L}$ can be found in Ref. 10, both the flow field velocity and adjoint velocity states solutions are required to compute induced velocities at any spatial point inside the rotor wake. Since the adjoint model solution diverges with forward time matching, the adjoint velocity state solution can only be obtained by integrating the adjoint model backward in time. However, the adjoint model only needs to be time marched backwards depending on how far into the wake is desired to capture rotor-to-rotor interactions. Even then, the additional complexity associated with the adjoint velocity solution makes the velocity potential model more challenging for integration into a real time flight dynamics model.

The coordinates definition used in the velocity potential flow model is shown in Fig. 1. In order to compute the velocity at point *a* (below the disk), velocities and adjoint velocities at various points are needed. Point *b* is the intersection point of the streamline and the rotor plane. Point *c* is centrosymmetric to point b on the disk plane while point *d* is centrosymmetric to point *a* but above the disk. The non-dimensional distance from point *a* along the streamline to point *b* is denoted by *s*. Now to compute the velocity at point *a* ($\vec{w}_a$), velocity at point *b* ($\vec{v}_b$) is added to the adjoint velocity at point *c* ($\vec{v}^*_c$) and then the adjoint velocity at point *d* ($\vec{v}^*_d$) is subtracted. In equation form, the induced velocity at any spatial point below the rotor disk in its wake is

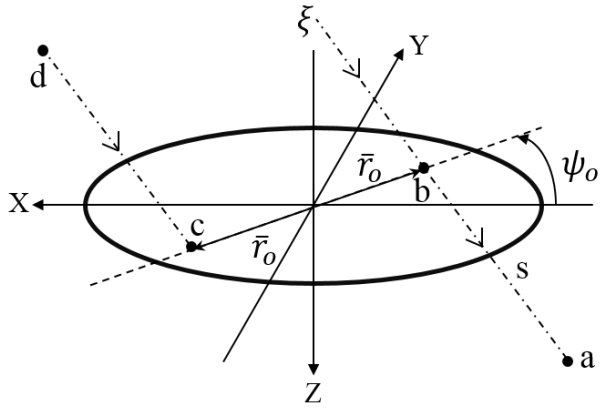


Figure 1: Coordinate system for computing induced velocity at point *a* inside the rotor wake (Ref. 6)

written as[10],

$$\begin{aligned}(21)\qquad \vec{w}_a(\bar{x},\bar{y},\bar{z},\bar{t}) &= \vec{w}_a(\bar{r},\psi,\bar{z},\bar{t}) \\ &= \vec{v}_b(\bar{r}_o,\psi_o,0,\bar{t}-s) \\ &+ \vec{v}_c^*(\bar{r}_o,\psi_o+\pi,0,\bar{t}-s) \\ &- \vec{v}_d^*(\bar{r}_o,\psi_o+\pi,-\bar{z},\bar{t})\end{aligned}$$

The velocity and adjoint velocity terms appearing on the right hand side of equation (21) are obtained using equation (19) with the state and co-state solutions of the model in equation (20).

## 4. METHODOLOGY FOR MODEL COMPARISON

In a coaxial rotor configuration, the lower rotor operates within the wake generated by the upper rotor. This means that the lower rotor experiences considerable aerodynamic interference from the upper rotor, affecting its performance. While the general case of model comparison involves the effects of individual load changes on resulting inflow changes at individual rotors, we focus this study on the effect of upper rotor load change on inflow change at the lower rotor. Furthermore, we also focus this study for hover flight condition as significant overlap of upper rotor wake at the lower rotor is present in hover.

### 4.1. Frequency responses from pressure and velocity potential superposition inflow models

A common approach for comparing dynamic responses from different models is through the frequency response plots. Each model is subjected to input signals of a range of frequencies and corresponding output responses are recorded. These signals are then post-processed using software such as CIFER® to generate the frequency responses. Differences in frequency responses between the models are measured using a single cost function, *J*[11] given as,

$$(22)\qquad J = \frac{20}{n_\omega}\sum_{\omega_1}^{\omega_{n_\omega}} W_\gamma[W_g(|\Delta T|)^2 + W_p(\angle\Delta T)^2]$$

In equation (22), $|\Delta T|$ is the magnitude difference in dB between the two models for comparison at each frequency, $\omega$. Similarly, $\angle\Delta T$ is the phase difference expressed in degrees at each frequency, $n_\omega$ is the number of frequency points and $\omega_1$ and $\omega_{n_\omega}$ are the starting and ending frequencies of fit, respectively. $W_\gamma$ is a weighting function dependent on the value of coherence function at each frequency, while $W_g$ and $W_p$ are relative weights for magnitude and phase comparisons, respectively. In Ref. 11, it is suggested to use $W_g = 1.0$ and $W_p = 0.01745$ which sets 1 dB magnitude error comparable with 7.57 degs phase error. As a guideline in flight dynamics modeling, a cost function of less than 50 means that differences between the two models is nearly indistinguishable in both frequency and time domains while a value of less than 100 generally reflects a good match between the models[11].

Both pressure and velocity potential superposition inflow models are implemented in MATLAB™ environment. A flowchart summarizing the steps to extract frequency responses from the inflow models is shown in Fig. 2. For both inflow models, steady-state inflow solutions corresponding to prescribed pressure loadings on both upper and lower rotors are obtained through time marching. Next, perturbations to individual pressure loading component are injected at the upper rotor for a period of time and corresponding inflow responses at a distance equal to the rotors' separation below the upper rotor are recorded. Input perturbation signals together with differences between the dynamic and steady-state inflow responses are converted to compatible form for use in CIFER® to generate the required frequency responses. For system identification purposes, a typical input chirp profile shown in Fig. 3 is used.

As stated before, this study considers upper rotor loading perturbation as input and the resulting inflow change at the lower rotor as output. Inflow states corresponding to the lower rotor are known directly from the pressure potential superposition inflow model solutions. However, in the velocity potential superposition inflow model, the states and co-states are intermediate quantities used to calculate the change in inflow velocity at the lower rotor using

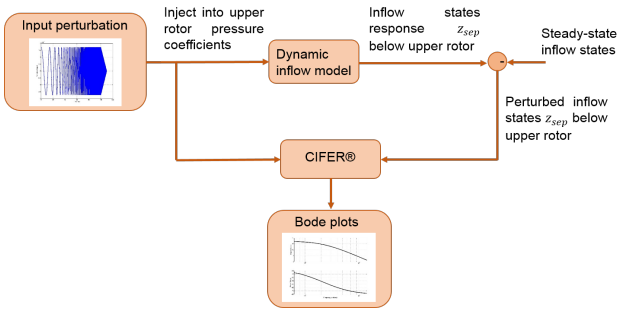


Figure 2: Flowchart on extraction of Bode plots from inflow models

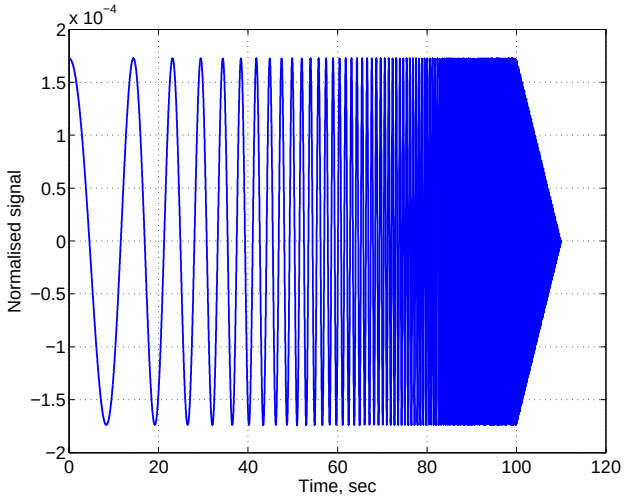


Figure 3: Profile of input perturbation used for system identification

equation (21). As such, velocities at selected locations on the lower rotor are first obtained from the velocity potential superposition inflow model. Using non-dimensional velocity ($\bar{v}_z$) and spatial location ($\bar{r}, \psi$) information at several preselected locations on the lower rotor, inflow states, i.e. uniform, fore-to-aft and side-to-side variations of inflow are computed using equation (23).

$$\alpha_1^0 = \frac{1}{2\pi}\int_0^{2\pi}\int_0^1 \bar{P}_1^0(\bar{r})\bar{v}_z(\bar{r},\psi)\bar{r}\,d\bar{r}\,d\psi \tag{23}$$

$$\alpha_2^1 = \frac{1}{\pi}\int_0^{2\pi}\int_0^1 \bar{P}_2^1(\bar{r})\bar{v}_z(\bar{r},\psi)\bar{r}\cos(\psi)\,d\bar{r}\,d\psi$$

$$\beta_2^1 = \frac{1}{\pi}\int_0^{2\pi}\int_0^1 \bar{P}_2^1(\bar{r})\bar{v}_z(\bar{r},\psi)\bar{r}\sin(\psi)\,d\bar{r}\,d\psi$$

### 4.2. Simulation setup

In general, the pressure potential superposition approach allows for an arbitrary number of inflow states. For ease of analysis, this study considers three inflow states consisting of uniform, fore-to-aft and side-to-side inflow variations; similar to the Pitt-Peters inflow model[12]. As such, each block in the M-matrix, i.e. $M_{11}, M_{12}, M_{21}, M_{22}$ has the structure shown in equation (24). In addition, each block in the L-matrix, $L_{11}, L_{12}, L_{21}, L_{22}$ has the same structure in equation (25). Lastly, the structure of the elements in $\alpha_1$, $\alpha_2$, $\tau_1$ and $\tau_2$ are defined in equation (26).

(24)
$$M_{ij} := \begin{bmatrix} m_{11} & 0 & 0 \\ 0 & m_{22} & 0 \\ 0 & 0 & m_{33} \end{bmatrix}_{ij} \qquad i = 1,2 \quad j = 1,2$$

(25)
$$L_{ij} := \begin{bmatrix} l_{11} & l_{12} & 0 \\ l_{21} & l_{22} & 0 \\ 0 & 0 & l_{33} \end{bmatrix}_{ij} \qquad i = 1,2 \quad j = 1,2$$

(26)
$$\alpha_i := \begin{Bmatrix} \alpha_1^0 \\ \alpha_2^1 \\ \beta_2^1 \end{Bmatrix}_i \qquad \tau_i := \begin{Bmatrix} \tau_1^{0c} \\ \tau_2^{1c} \\ \tau_2^{1s} \end{Bmatrix}_i \qquad i = 1,2$$

The numbers of flow field velocity states and adjoint velocity states (co-states) in the velocity potential inflow model are each set to three for each rotor. As such, there are a total of twelve states for the model based on the velocity potential superposition method.

Geometric properties from the Harrington coaxial rotor[13] is used in this study. The rotor radius is 12.5 ft and upper rotor is offset from the lower rotor by 2.38 ft (19 percent of rotor radius). The rotational speed of both upper and lower rotors is 37.5 rad/s.

Both pressure and velocity potential superposition inflow models are time marched to steady-state for 10 seconds with prescribed pressure loadings on upper and lower rotors. Next, chirp perturbation signal with magnitude equivalent to thrust coefficient of 0.0002 and frequency ranging from 0.05 to 4.5 Hz over a period of 100 seconds is injected into each model. Towards the end of the frequency sweep, the input signal magnitude is reduced linearly to zero as shown in the last 10 seconds of the plot in Fig. 3. This prevents exciting frequencies beyond the range of interest since an abrupt change in input perturbation is similar to a step change.

## 5. RESULTS

A comparison of the time responses between pressure and velocity potential superposition inflow

models to step perturbation in upper rotor uniform loading is studied first. The steady-state inflow solutions correspond to upper and lower rotors steady-state thrust coefficients of 0.0032 and 0.0027, respectively. In Fig. 4, input perturbation is upper rotor uniform pressure coefficient and output is the resulting variation in induced velocity at an arbitrary point on the lower rotor. From the transient response, time delay is seen for the curve corresponding to velocity potential superposition inflow model when compared to the results from the pressure potential superposition inflow model.

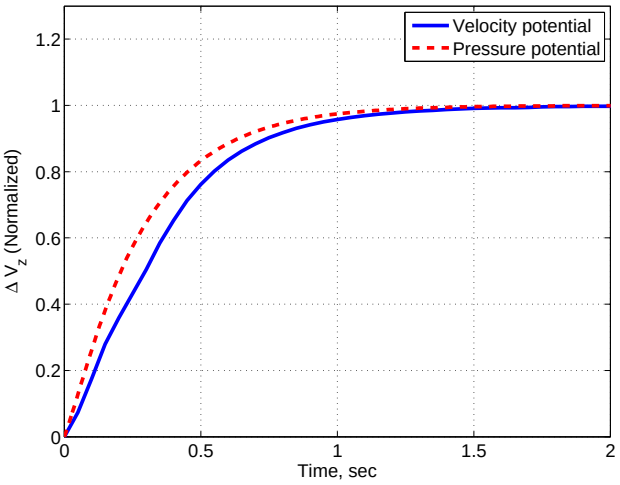


Figure 4: Inflow change at lower rotor due to step change in upper rotor uniform pressure coefficient

In Fig. 5, time responses of both models subjected to upper rotor fore-to-aft pressure coefficient perturbation is shown. Similar to the uniform inflow state transient response, velocity potential superposition inflow model shows time delay effects in the transient response.

Transient time responses predicted by velocity potential superposition inflow model at different distances below the rotor is studied and the results are shown in Fig. 6. For illustration purposes, only step perturbation to upper rotor uniform pressure coefficient is shown since perturbation to other components exhibit similar trends. It is observed that initial delay in inflow response at the lower rotor increases with increasing separation distance ($z_{sep}$) between the rotors.

An estimate of the time delay may be obtained by considering a single state representation in the velocity potential model. Consider the use of equation (21) for computing vertical component of the flow field in the wake of upper rotor ($w_z$) at an axial distance $\bar{z}$ below the rotor and at a non-dimensional time $\bar{t}$.

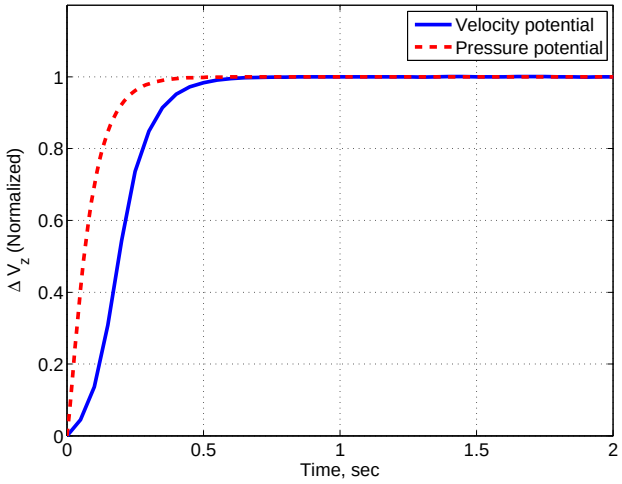


Figure 5: Inflow change at lower rotor due to step change in upper rotor fore-to-aft pressure coefficient

Equation (21) for this case simplifies to,

$$w_z(\bar{z},\bar{t}) = v_z(0,\bar{t}-\bar{z}) + v_z^*(0,\bar{t}-\bar{z}) - v_z^*(-\bar{z},\bar{t}) \tag{27}$$

In order to examine the dynamic response of the flow below the rotor due to changes in the rotor's pressure loading, each term on the right-hand-side of equation (27) can be found by solving the state and co-state equations of the velocity potential model (equation (20)) subject to a step input to the uniform pressure coefficient of the upper rotor. The resulting solution may be approximated with time constant $\eta$ as shown in equation (28).

$$w_z(\bar{z},\bar{t}) = \begin{cases} e^{-\eta(\bar{z}-\bar{t})} - e^{-\eta\bar{z}}, & 0 < \bar{t} < \bar{z} \\ 2 - e^{-\eta\bar{z}} - e^{-\eta(\bar{t}-\bar{z})}, & 0 < \bar{z} < \bar{t} \end{cases} \tag{28}$$

Interestingly, the form of the approximated solution for the simplified case given in equation (28) suggests the presence of time delay effect in the response. In a coaxial rotor system, this means that a change in upper rotor pressure loading has a delayed effect on interference velocities experienced by the lower rotor and is dependent on the rotors' separation distance. Since the time delay is expressed as non-dimensional reduced time, its dimensional form can be recovered by using the rotors' separation distance and total average flow at the rotor (as $V_\infty$ is zero for hover). As such, for a given coaxial rotor configuration, the time delay ($t_d$) can be estimated given the rotors' separation distance ($z_{sep}$) and the total average flow ($V_T$) as,

$$t_d = \frac{z_{sep}}{V_T} \tag{29}$$

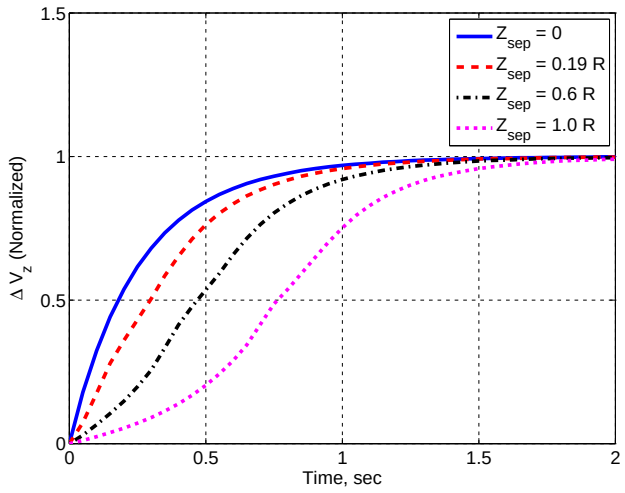


Figure 6: Velocity potential superposition inflow model time response at different distances below rotor due to step change in upper rotor uniform pressure coefficient

From equation (29), time delay increases with separation distance between upper and lower rotors. This prediction agrees well with the results shown in Fig. 6.

### 5.1. Frequency response comparisons

Bode plot comparisons between pressure and velocity potential superposition inflow models are shown in Fig. 7. Similar to the step response case, the upper and lower rotors have steady-state thrust coefficients of 0.0032 and 0.0027, respectively. Input perturbation is upper rotor uniform pressure coefficient and output is lower rotor uniform inflow state. From the magnitude plot, both inflow models have the same magnitude responses at frequencies less than 2 rad/s.

For phase plot, there are significant differences between the pressure and velocity superposition inflow models across the frequencies considered. An important observation is that the phase for velocity potential model begins to roll off as frequency increases. This is due to the presence of time delay in the system which the velocity potential superposition inflow model is able to capture. The time delay can be explained by the fact that inflow perturbations from upper rotor take a finite amount of time to propagate downstream within the wake to the lower rotor. On the other hand, pressure potential superposition inflow model as formulated does not capture this time delay effect as its phase is seen to be asymptotic at -90$^o$, typical of a first order system phase response without any time delay. The frequency response cost function ($J$) is 140.2, of which 28.3 is due to differences in magnitude response while 111.9 is due to differences in phase response.

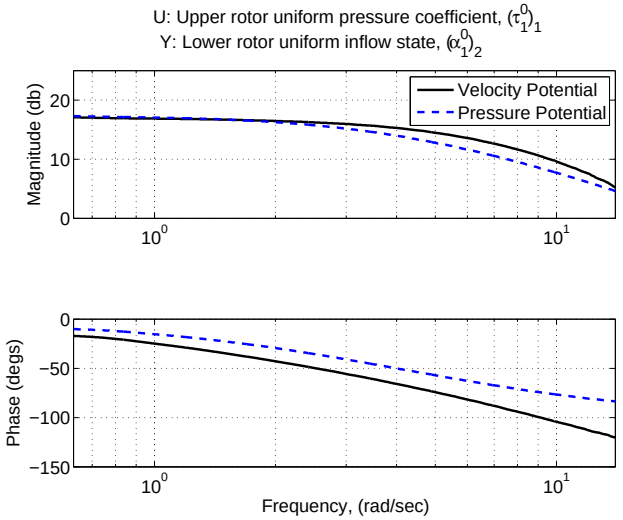


Figure 7: Comparison of frequency responses of uniform inflow state at lower rotor due to upper rotor uniform pressure coefficient between pressure and velocity potential superposition models

## 6. CONCLUDING REMARKS

A finite state inflow model for coaxial rotor system has been developed from single rotor formulation. The single rotor pressure and velocity potential inflow models are extended to the case of a coaxial rotor system using the superposition method.

Both time and frequency response comparisons between the pressure and velocity potential superposition inflow models of a coaxial rotor system using geometric parameters of the Harrington rotor are performed. In order to assess rotor-to-rotor flow field coupling in hover, changes in lower rotor inflow due to perturbations in upper rotor pressure coefficients are analyzed as the lower rotor operates in the wake of the upper rotor. For step perturbation to upper rotor pressure coefficient, differences in transient time responses between pressure and velocity potential models are observed. In addition, the Bode plots reveal that there are significant phase differences between the two models. Both the time and frequency response results show that the velocity potential superposition inflow model captures the time delay present in the system as upper rotor inflow perturbations take time to propagate downstream to the lower rotor. This time delay effect is missing in the formulated pressure potential superposition inflow model of a coaxial rotor system.

The next step is to incorporate time delay elements

in the rotor-to-rotor coupling terms in the pressure potential superposition inflow model and re-evaluate the new model using time and frequency response analyses.

## 7. ACKNOWLEDGMENTS

This study is supported under the NRTC Vertical Lift Rotorcraft Center of Excellence (VLRCOE) from the U.S. Army Aviation and Missile Research, Development and Engineering Center (AMRDEC) under Technology Investment Agreement W911W6-06-2-0002, entitled National Rotorcraft Technology Center Research Program. The authors would like to acknowledge that this research and development was accomplished with the support and guidance of the NRTC. The views and conclusions contained in this document are those of the authors and should not be interpreted as representing the official policies, either expressed or implied, of the AMRDEC or the U.S. Government. The U.S. Government is authorized to reproduce and distribute reprints for Government purposes notwithstanding any copyright notation thereon.

## 8. REFERENCES

[1] Peters, D. and He, C., "Finite state induced flow models part II: Three-dimensional rotor disk," *Journal of Aircraft*, vol. 32, Mar. 1995.

[2] Advanced Rotorcraft Technology, Inc., *FLIGHTLAB X-Analysis user manual*, July 2013.

[3] US Army Research, Develompment, and Engineering Command, *Rotorcraft Comprehensive Analysis System user's manual*, Aug. 2012.

[4] Morillo, J. and Peters, D. A., "Velocity field above a rotor disk by a new dynamic inflow model," *Journal of Aircraft*, vol. 39, pp. 731–738, Oct. 2002.

[5] Fei, Z. and Peters, D. A., "A rigorous solution for finite-state inflow throughout the flowfield," The 30th AIAA Applied Aerodynamics conference, New Orleans, Louisiana, 2012.

[6] Fei, Z. and Peters, D. A., "Inflow below the rotor disk for skewed flow by the finite-state, adjoint method," 38th European Rotorcraft Forum, 2012.

[7] Prasad, J. V. R., Nowak, M., and Xin, H., "Finite state inflow models for a coaxial rotor in hover," in *Proceedings of the 38th European Rotorcraft Forum*, Sept. 2012.

[8] Nowak, M., Prasad, J. V. R., Xin, H., and Peters, D. A., "A potential flow model for coaxial rotors in forward flight," in *Proceedings of the 39th European Rotorcraft Forum, Moscow, Russia*, 2013.

[9] Nowak, M., Prasad, J. V. R., and Peters, D., "Development of a finite state model for a coaxial rotor in forward flight," in *Proceedings of the AHS 70th annual Forum*, May 2014.

[10] Fei, Z., *A rigorous solution for finite-state inflow throughout the flowfield*. PhD thesis, Washington University in St. Louis, May 2013.

[11] Tischler, M. B. and Remple, R. K., *Aircraft and Rotorcraft System Identification*. American Institute of Aeronautics, 2012.

[12] Pitt, D. M. and Peters, D. A., "Theoretical prediction of dynamic inflow derivatives," *Vertica*, vol. 5, Mar. 1981.

[13] Harrington, R., "Full scale tunnel investigation of the static thrust performance of a coaxial helicopter rotor," NACA TN 2318, Mar. 1951.